

Hydrate formation and growth in pores

Jong-Won Jung*, J. Carlos Santamarina

Georgia Institute of Technology, Civil & Environmental Engineering, 790 Atlantic Drive N.W., Atlanta, GA 30332-0355, United States

ARTICLE INFO

Article history:

Received 21 December 2010

Received in revised form

18 January 2012

Accepted 29 January 2012

Communicated by Y. Furukawa

Available online 8 February 2012

Keywords:

A1. Crystal morphology

A1. Growth models

A1. Nucleation

ABSTRACT

Gas hydrates consist of guest gas molecules encaged in water cages. Methane hydrate forms in marine and permafrost sediments. In this study, we use optical, mechanical and electrical measurements to monitor hydrate formation and growth in small pores to better understand the hydrate pore habit in hydrate-bearing sediments. Hydrate formation in capillary tubes exposes the complex and dynamic interactions between nucleation, gas diffusion and gas solubility. The observation of hydrate growth in a droplet between transparent plates shows that the hydrate shell does not grow homogeneously but advances in the form of lobes that invade the water phase; in fact, the hydrate shell must be discontinuous and possibly cracked to justify the relatively fast growth rates observed in these experiments. Volume expansion during hydrate formation causes water to flow out of menisci; expelled water either spreads on the surface of water-wet substrates and forms a thin hydrate sheet, or remains next to menisci when substrates are oil-wet. Hydrate formation is accompanied by ion exclusion, yet, there is an overall increase in electrical resistance during hydrate formation. Hydrate growth may become salt-limited in trapped water conditions; in this case, aqueous brine and gas CH₄ may be separated by hydrate and the three-phase system remains stable within the pore space of sediments.

© 2012 Elsevier B.V. All rights reserved.

1. Introduction

Gas hydrate consists of guest gas molecules encaged in water cages under the high fluid pressure and low temperature. In nature, methane gas hydrates are found in sediments under high pore pressure and low temperature. The low solubility of methane in water (e.g. 1CH₄ in ~800H₂O molecules) contrasts with the high concentration of methane in hydrate (1CH₄ every 6H₂O). Several laboratory methods have been developed to circumvent the long time required for diffusion-limited hydrate formation in sediments, such as flushing methane gas through partially water-saturated sediments [1,2], advecting gas dissolved in water [3], and mixing ground ice to exploit the presence of pre-existing ice cages [4–11], and pre-mixing ground hydrate with the sediments [12].

Each of these methods produces different hydrate patterns in pore-scale [5,13–15], which eventually affect the macro-scale mechanical properties of hydrate-bearing sediments [16]. For example, even a small amount of hydrate at interparticle contacts causes a much higher increase in the small strain stiffness of hydrate-bearing sediments, as compared to the same hydrate mass resting within the pore space [16,17].

The purpose of this study is to investigate hydrate formation and growth patterns including hydrate shapes and growth rates

on water-wet and oil-wet substrates, and to explore the effect of salts when the water volume is limited in a closed system.

2. Preliminary concepts

2.1. Hydrate nucleation on surfaces

Preferential hydrate nucleation on substrates, i.e., heterogeneous nucleation, can be explained in thermodynamic terms using the concept of Gibbs free energy. The change in Gibbs free energy from water to hydrate ΔG is lower when hydrate forms on substrates ΔG^* than when it forms in the bulk water ΔG . The value of ΔG^* varies according to particle characteristics such as composition, crystallography, and surface charge [18]. It can be related to the bulk water ΔG through the contact angle between the liquid, gas hydrate, and the mineral [19]

$$\Delta G^* = \Delta G \left[\frac{1}{4} (2 + \cos \theta) (1 - \cos \theta)^2 \right]^{1/3} \quad (1)$$

The contact angle relates the interfacial tensions γ (J m⁻²) between mineral and liquid γ_{ml} , mineral and hydrate γ_{mh} , and hydrate and liquid γ_{hl} .

$$\cos \theta = \frac{\gamma_{ml} - \gamma_{mh}}{\gamma_{hl}} \quad (\text{Young's equation}) \quad (2)$$

Molecular dynamic simulations corroborate thermodynamic predictions and provide molecular-scale insight. In particular,

* Corresponding author. Tel.: +1 404 643 6261; fax: +1 404 894 2281.

E-mail addresses: jwjung7695@gmail.com, kocee76@hotmail.com (J.-W. Jung).

these simulations show lower activity near substrates and early water structuring that favors hydrate nucleation (see simulations in Kvamme et al., 2007 [20] and Walsh et al., 2009 [21]).

2.2. Hydrate growth

After nucleation, hydrate grows forming a thin shell along the water–gas interface [2,23]. Then, it starts to grow into the liquid phase as shown by water droplet tests [22,24–28] and gas–water tests in tubes [23,25,27,29–37]. It is generally thought that the hydrate growth rate is gas diffusion controlled. Gas diffusion is low in water ($D=1.37\text{--}1.49 \times 10^{-9} \text{ m}^2/\text{s}$ —Thomas [38]; Withersp and Bonoli [39]) and even lower through the CH_4 hydrate mass ($D=3.4 \times 10^{-13} \text{ m}^2/\text{s}$ —Davies and Fear[40]). Hydrate may also grow into the gas phase forming a tree-branch geometry as water escapes confined liquid volumes [41].

2.3. Gas solubility and Ostwald ripening

Hydrate dissolution occurs inside the hydrate stability field when the water that surrounds the hydrate mass is not gas-saturated [42,43]. Gas solubility in bulk water at 6.6 MPa and 274 K is 1.66 mol/kg for CO_2 and 0.12 mol/kg for CH_4 . However, gas solubility decreases when hydrate is present [44–47]; for example, it falls to 0.83 mol/kg for CO_2 , and to 0.063 mol/L for CH_4 at 6.6 MPa and 274 K [48].

Gas concentration increases near small hydrate nuclei. Therefore, a concentration gradient develops between the water that surrounds a small crystal and a nearby large one. Eventually, diffusive transport leads to the growth of large crystals at the expense of small ones. This process is known a Ostwald ripening [49,50].

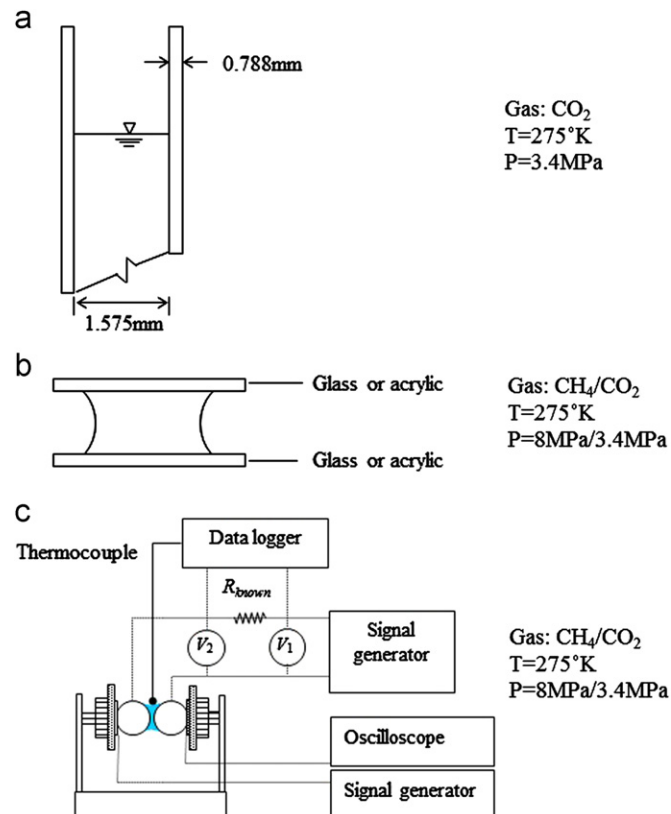


Fig. 1. Experimental device. Hydrate formation and growth. (a) In a capillary tube, (b) between hydrophilic (glass) or hydrophobic (acrylic) plates and (c) between two copper spheres.

2.4. Ion exclusion

Finally, we note that the formation of hydrate cages during slow hydrate formation displaces nearby hydrated ions which must diffuse back into the liquid water [51–54].

3. Experimental study

Three sets of experiments are conducted to study hydrate formation near substrates. All experiments are monitored using time-lapse photography (resolution: 1 pixel $\sim 10 \mu\text{m}$), pressure transducers and thermocouples. Tests are conducted inside P-T controlled pressure chambers. Experimental devices, materials, and procedure are described next (refer to Fig. 1).

3.1. Hydrate in capillary tubes (Fig. 1a)

In this study, the capillary tube is its own pressure chamber (polyphenylsulfone; rated for 106 MPa; outside diameter 3.15 mm; inside diameter 1.57 mm). The contact angle between distilled water and the capillary tube is near $\sim 90^\circ$. First, we fill the tube with degassed water until the water–air interface is centered in the field of view; then, the tube is placed in a cooler at $\sim 275 \text{ K}$, and is pressurized to $\sim 3.4 \text{ MPa}$ with CO_2 gas.

3.2. Hydrate formation between water-wet or oil-wet surfaces (Fig. 1b)

Transparent glass and acrylic plates are used to simulate water-wet and oil-wet surfaces. A water droplet is placed between two parallel glass or acrylic plates creating a quasi-

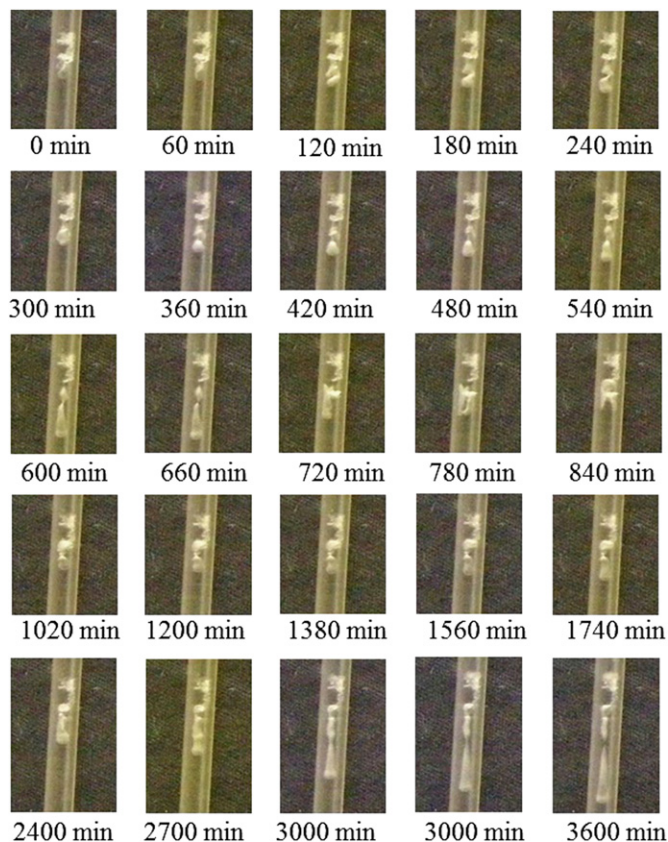


Fig. 2. Hydrate formation and growth in capillary tubes. The first image corresponds to the first observation of hydrate formation after a long induction time of ~ 14 days. The time for subsequent images is referenced to the first one.

cylindrical body of water [e.g. 8.7 mm diameter, 1.97 mm in height (distance between two plates), and 120 mg water mass]. Water droplets with various salinities between 0 M and 1.28 M NaCl are tested. This parallel-plate device is placed inside a stainless steel pressure chamber (thickness ~43 mm; design pressure ~30 MPa) that has a large size sapphire window for visual observation (70 mm diameter) and multiple feed through ports for instrumentation. The chamber is maintained at ~275 K and it is pressurized to ~8 MPa for CH₄ hydrate formation studies and to ~3.4 MPa for CO₂ hydrate formation studies. Nucleation is triggered by causing transient ice formation at low temperature

(258–263 K); thereafter, constant temperature (~275 K) and pressure (~3.4 MPa or ~8 MPa) conditions are maintained during the test.

3.3. Hydrate formation in a water meniscus between spherical particles (Fig. 1c)

In this third set of tests, a droplet of salt water (NaCl; various concentrations between 0 M and 1.28 M) is placed between two copper spheres, creating a geometric configuration similar to that of a naturally occurring water meniscus between two non-touching grains (copper sphere: 5.2 mm diameter, water droplet: 3.4–4.1 mm in diameter, 1.3–1.89 mm in height, and 12–25 mg in mass). The copper spheres are glued onto cylindrical piezocrystals. This configuration allows us to measure electrical resistance and relative stiffness during hydrate formation. Fig. 1c shows the electrical circuit and peripheral electronics used. Electrical resistance is determined at 50 kHz to avoid electrode polarization effects. The resistance of the meniscus R is a function of the measured voltages V_1 and V_2 (Fig. 1c), and the known resistance of the series resistor $R^*=4700 \Omega$,

$$R = \frac{V_2}{V_1 - V_2} R^* \quad (3)$$

The source piezocrystal is connected to a sinusoidal signal generator operated at ~60 kHz. The signal amplitude produced by the output piezocrystal is measured using an oscilloscope. The test device is placed inside a pressure chamber and is subjected to P–T conditions similar to the previous test except that no transient ice formation is used to trigger hydrate nucleation; therefore, these tests experienced long induction times.

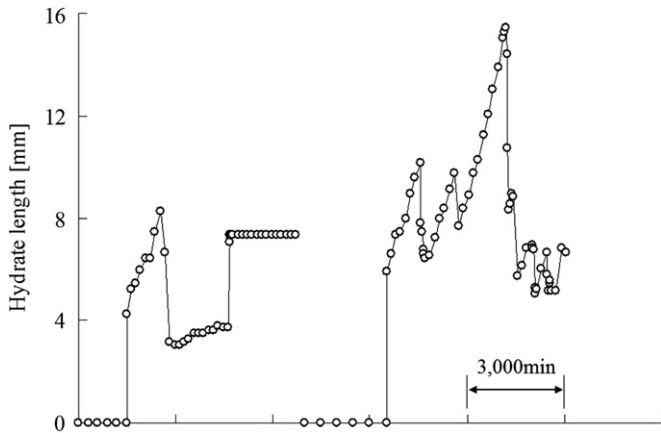


Fig. 3. Rate of hydrate formation in capillary tubes. Data are shown for two typical experiments [Note. Hydrate length is obtained by sum of discontinuous hydrate length which is the distance from top and bottom of each hydrate in Fig. 2].

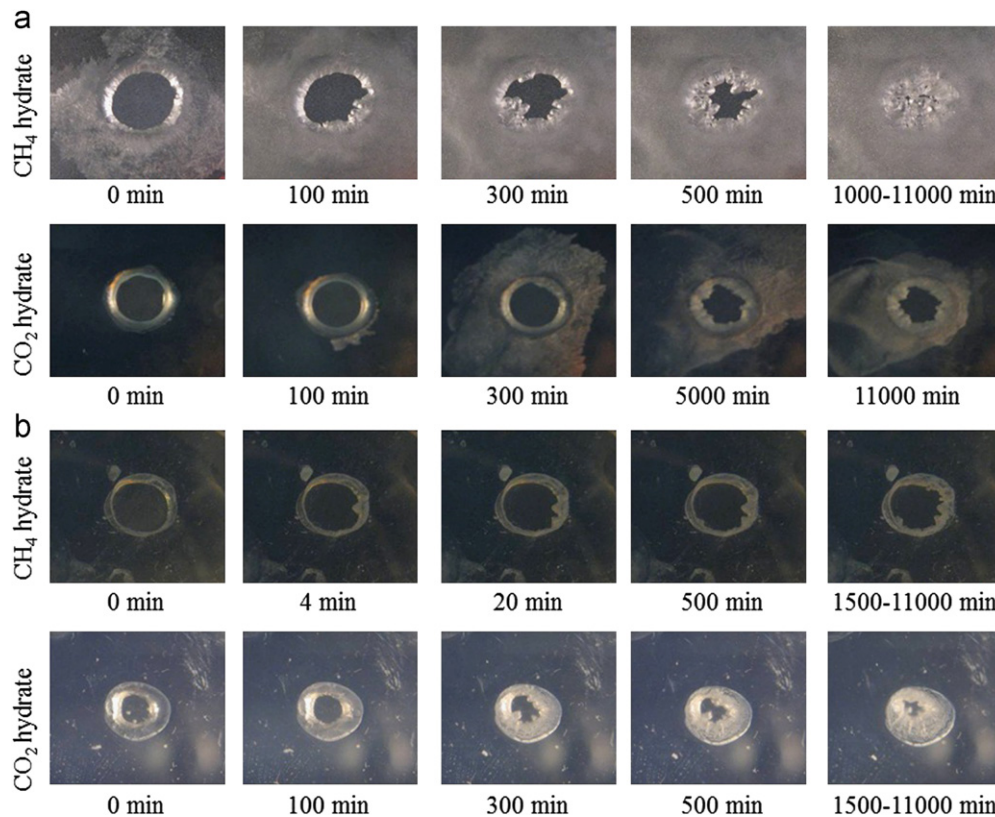


Fig. 4. Hydrate formation and growth—Meniscus between two surfaces. The first image in each sequence corresponds to the first observation of hydrate formation and it is assigned time $t=0$ min. The time for subsequent images is referenced to the first one. (a) Hydrophilic, water-wet glass substrates and (b) hydrophobic, oil-wet acrylic substrates.

4. Experimental results

4.1. Hydrate formation in capillary tubes

A collection of images gathered during a single test is presented in Fig. 2. Multiple similar tests allow us to make the following observations. Hydrate nucleates suddenly at the interface between the gas and water phases after long induction times (after ~ 14 days). Growth into the water phase is rather discrete, i.e. in steps (Fig. 3). Hydrate also grows into the gas phase in part due to the water volume expansion during water-hydrate transformation ($V_{hyd}/V_w=1.279$). We often see that a fraction of the hydrate mass dissolves after some growth and begins to re-grow. Hydrate dissolution-growth cycles repeat multiple times with an overall growth-trend. The hydrate mass is elongated, and does not adhere to the plastic capillary tube.

4.2. Hydrate formation between water-and oil-wet substrates

The evolution of hydrate formation in the water droplet between the two parallel plates is documented in Fig. 4. Nucleation is triggered

by causing transient ice formation to prevent long induction times; hydrate nucleates at the gas-water interface after ice melts (see also Jung and Santamarina [55]). Hydrate does not grow homogeneously but advances in the form of lobes that invade the water meniscus. Volume expansion during hydrate growth causes water to flow out of the meniscus. The displaced water coats water-wet surfaces and forms a thin hydrate layer on them (Fig. 4a); however, water does not flow away from meniscus onto hydrophobic surface (Fig. 4b). When salt solutions are used, water trapped inside the meniscus may not change into hydrate (observation times as long as $\sim 11,000$ min), and remains as liquid water surrounded by the hydrate shell that separates the gas phase from the liquid water. In all cases, hydrate appears suddenly (within the time interval of two successive images $\Delta T=10$ s), but grows slowly as a shown in Fig. 5.

4.3. Hydrate formation at menisci between grains

The chamber P-T conditions, the meniscus electrical resistance and changes in stiffness during hydrate formation and dissociation are monitored in this set of tests (Fig. 6). We do not observe a pressure drop during formation (circle in Fig. 6a) because the

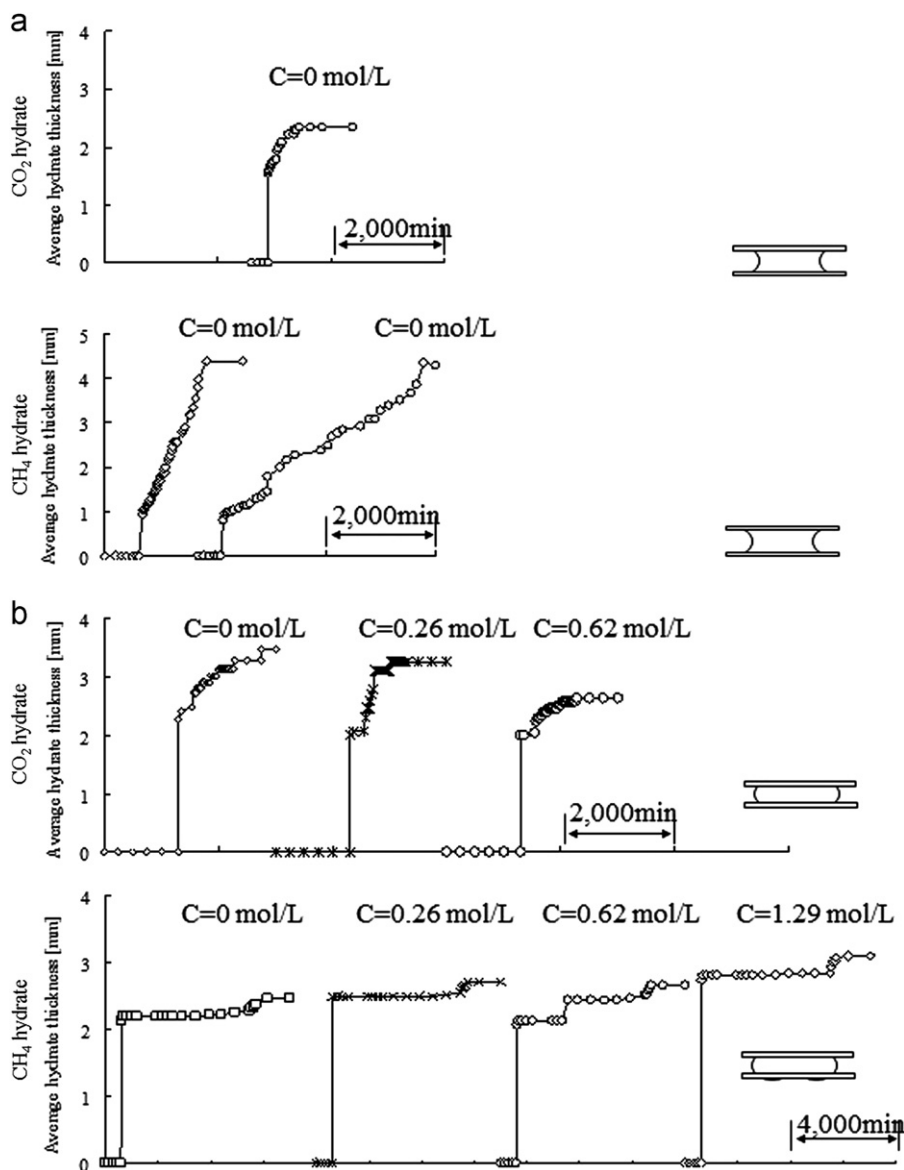


Fig. 5. Rate of hydrate formation between plates. (a) Hydrophilic water-wet plates and (b) hydrophobic oil-wet plates. Data for CO₂ and CH₄ hydrates.

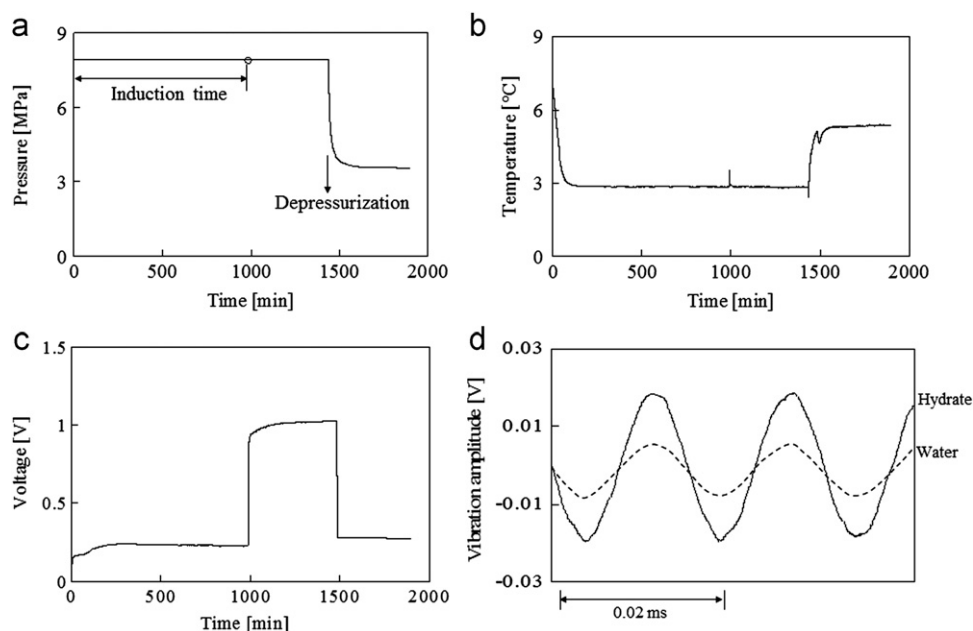


Fig. 6. CH₄ hydrate formation at a water meniscus between two particles—Salt solution (NaCl 0.26 mol/L). (a) Pressure, (b) temperature, (c) voltage drop across the meniscus (used for calculating electrical resistance) and (d) instantaneous vibration amplitude detected by the receiving piezocrystal (used for relative stiffness estimation).

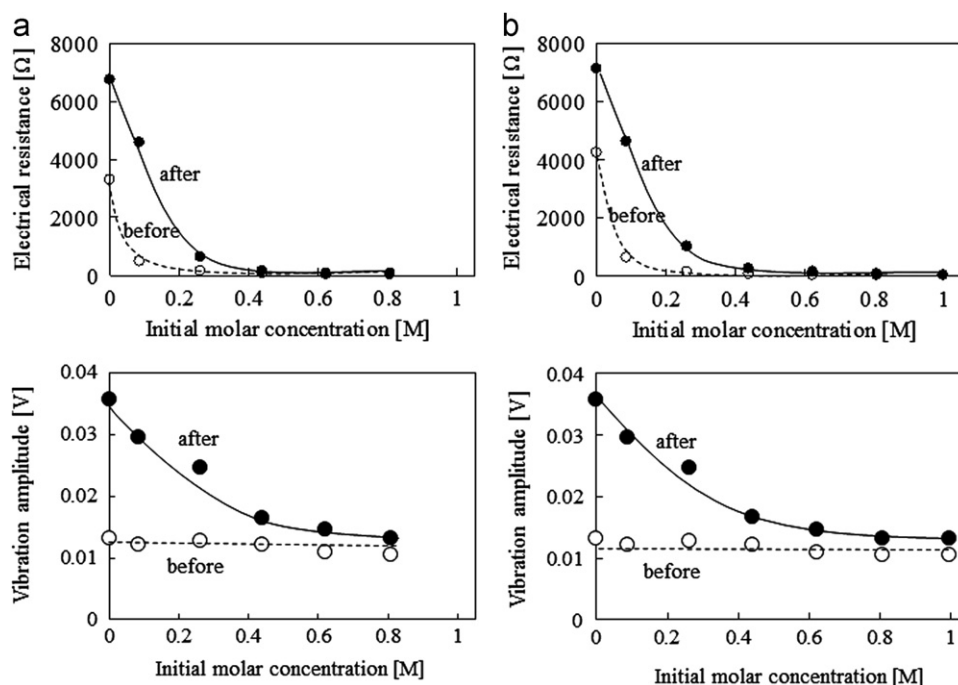


Fig. 7. Change in the meniscus electrical resistance and relative stiffness before and after hydrate formation. Solutions with different initial ionic concentration. (a) CH₄ hydrate and (b) CO₂ hydrate.

chamber volume is much larger than the volume of water in the meniscus (approximately $\sim 17,000$ times larger). Hydrate formation causes ion exclusion; in turn, hydrate growth is hindered by high salt concentration. These two processes define the evolution of electrical resistance and stiffness in these experiments. The initial electrical resistance is lower in drops with higher salt concentration; in all cases, electrical resistance increases after hydrate formation. The change in electrical resistance before and after hydrate formation (both CO₂ and CH₄) decreases as the salt concentration increases (Fig. 7).

The strength of the transmitted mechanical vibration is not sensitive to salt concentration before hydrate formation. The

sensing piezocrystal output increases after hydrate formation. The increase in mechanical transmission is more pronounced when the initial salt concentration is low as shown in Fig. 7 (both CO₂ and CH₄ hydrate).

5. Analyses and discussion

5.1. Fast early hydrate growth

The sudden formation of an initial hydrate mass is faster than that can be justified by concurrent gas diffusion through (e.g.,

results in Fig. 5). Let us compute the initial hydrate thickness in terms of (1) the saturation concentration of methane in water before hydrate formation C_{bh} assuming that the induction time for nucleation exceeds the diffusion time ($C_{bh}=0.12$ mol/kg for CH_4 –275 K, 8 MPa and 1.39 mol/kg for CO_2 –275 K, 3.4 MPa), (2) the gas concentration after hydrate formation C_{ah} ($C_{ah}=0.063$ mol/kg for CH_4 –275 K, 8 MPa and 0.89 mol/kg for CO_2 –275 K, 3.4 MPa), and (3) the gas concentration in hydrate ($C_h=8.06$ mol/kg for CH_4 hydrate and 6.57 mol/kg for CO_2 hydrate for a hydration number $n=6$). Then, the conservation of gas molecules requires (Fig. 8),

$$\pi R^2 \rho_w C_{bh} - \pi (R-h)^2 \rho_w C_{ah} = [\pi R^2 - \pi (R-h)^2] \rho_h C_h \quad (4)$$

The estimated initial hydrate thickness that can form by consuming the dissolved gas is $h=0.16$ μm in CH_4 and $h=136$ μm in CO_2 hydrate (for a water droplet radius $R=4.3$ mm, water density $\rho_w=1$ g/cm³ and hydrate density $\rho_{h,\text{CO}_2}=1.11$ g/cm³, $\rho_{h,\text{CH}_4}=0.94$ g/cm³) [Note. The hydrate thickness (~ 2 mm) measured in Fig. 5 is overestimated due to the shape of water droplet which is not perfect cylindrical shape].

5.2. Hydrate dissolution—transients

Gas diffuses into the water mass during the induction time (Fig. 9a and b). Then, rapid hydrate growth takes place and consumes the excess gas $C_{bh}-C_{ah}$ that dissolved during the induction time, as discussed above (Fig. 9c). After this initial hydrate formation stage, gas continues diffusing into the liquid water from the gas phase supporting further hydrate growth (path I—Fig. 9c). At the same time, diffusion tends to homogenize

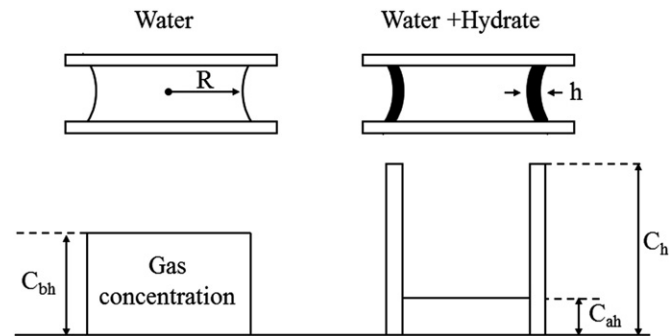


Fig. 8. Fast early hydrate formation by the consumption of excess gas ($C_{bh}-C_{ah}$). (a) Before hydrate formation and (b) after hydrate formation. Note: CO_2 gas solubility in water at 3 MPa, 273 K is: $C_{ah}=0.06$ mol/kg with hydrate and $C_{bh}=0.11$ mol/kg without hydrate.

the gas concentration at the lower tip of the hydrate mass (path II in Fig. 9c); this second transport process causes dissolution at the tip. The coexistence of these two processes explains the transient formation–dissolution cycles during the first few hours, and the overall increase in hydrate mass observed in tube experiments (see Fig. 3).

5.3. Hydrate growth on different substrates

5.3.1. Water–mineral interaction

All our data show that hydrate growth in pores takes place in discrete steps rather than gradually. Hydrate growth rate can be obtained by thickness increase after initial hydrate nucleation. The CO_2 hydrate growth rate in the context of oil-wet surfaces is between 0.38 $\mu\text{m}/\text{min}$ and 0.74 $\mu\text{m}/\text{min}$ (Fig. 5). The hydrate growth rate in the meniscus between water-wet surfaces is higher (0.9–1.9 $\mu\text{m}/\text{min}$) than that between oil-wet surfaces. Hence, hydrate growth is affected by sediment surface boundaries (Fig. 10).

5.3.2. Shell breakage

Very slow growth rates are anticipated for diffusive gas transport through the hydrate shell. However, the fast growth rates observed in these experiments suggest that gas must reach the water inside the meniscus through discontinuities in the hydrate shell that separates the gas from the liquid water (Fig. 5). Our complementary FEM simulations of hydrate formation around the water droplet confirm the formation of tensile fractures in the hydrate shell due to water-to-hydrate expansion ($V_{\text{hyd}}/V_w=1.23$ –1.28).

5.3.3. Hydrate growth topology

Hydrate does not grow homogeneously as a planar front but advances in the form of lobes that invade the water phase. Tensile fractures in the hydrate shell may explain lobe formation in menisci (Fig. 4); however, this is not the case in capillary tubes shown in Fig. 2. This elongated hydrate topology exhibits a higher surface area than a planar front and is consistent with hydrate formation by gas from supersaturated water: there is a shorter distance for diffusive transport to these long lobes than to a planar front. This shorter diffusive distance causes a faster initial hydrate growth (3.6–5.3 $\mu\text{m}/\text{min}$) than a planar front growth. Higher surface area also favors heat diffusion following phase transformation [36].

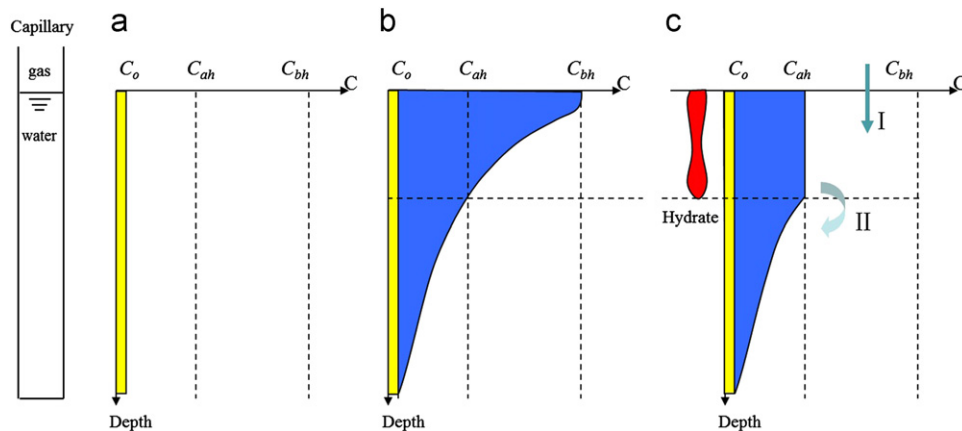


Fig. 9. Changes in gas concentration within a capillary tube. (a) Initial gas concentration, (b) after gas diffusive transport during the induction time and (c) immediately after sudden hydrate formation. Note: CO_2 gas solubility in water at 3 MPa, 273 K is: $C_{ah}=0.06$ mol/kg with hydrate and $C_{bh}=0.11$ mol/kg without hydrate.

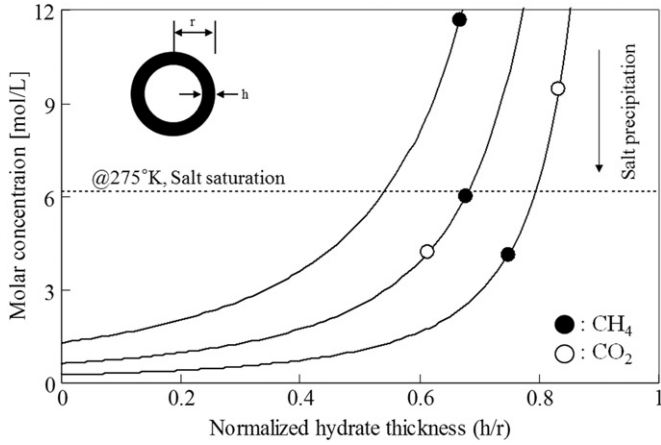


Fig. 10. Change in salt concentration by ion exclusion as a function of hydrate thickness (closed system, i.e., mass conservation). Lines show the increase in salt concentration in the remaining free water during hydrate growth. The dotted line shows the salt concentration saturation at 275 K. Points represent final hydrate thickness and molar concentration estimated for the experiments reported in Fig. 7. Salt precipitation is anticipated.

5.4. Relative stiffness and electrical resistivity

Relative stiffness measurements can be analyzed assuming a mechanical system made of three springs in series held between fixed boundaries to represent the source piezocrystal, the meniscus, and the receiver piezocrystal. The relative amplitude between the input V_i and output V_o voltages is a function of the displacement in the input piezocrystal δ_i and the output piezocrystal δ_o . The latter one depends on the meniscus response $\delta_m \approx \delta_o - \delta_i$ through a function that combines the stiffness of piezocrystals k_{piezo} , the meniscus height L_m , the medium Young’s modulus E_m , and the area of the meniscus A_m ,

$$\frac{V_o}{V_i} = \alpha \frac{\delta_o}{\delta_i} = \alpha \frac{\delta_o}{\delta_o + \delta_m} = \alpha \frac{1}{1 + \frac{k_{piezo}L}{E_m A_m}} \quad (5)$$

Therefore, the relative amplitude V_o/V_i reflects the evolution of the meniscus stiffness during hydrate formation. Electrical current flows through the free water that remains inside the hydrate shell. Therefore, when an annular CH_4 hydrate shell forms, the measured resistance reflects the contributions of water and hydrate [55]. Electrical resistance R is a function of resistivity ρ , meniscus length L_m area A_m , and a shape factor β ,

$$\frac{1}{R_{water+hyd}} = \frac{1}{R_{hyd}} + \frac{1}{R_{water}} = \frac{1}{\beta L_m} \left(\frac{A_{hyd}}{\rho_{hyd}} + \frac{A_m - A_{hyd}}{\rho_{water}} \right) \approx \frac{1}{\beta L_m} \frac{A_m - A_{hyd}}{\rho_{water}} \quad (6)$$

The simplification in the last equality recognizes that the electrical conductivity of hydrate is much lower than the conductivity of salt water.

The relative amplitude V_i/V_o from the mechanical excitation (Eq. (5)) and electrical resistance $R_{water+hyd}$ (Eq. (6)) are proportional to the hydrate area A_{hyd} . The analysis of experimental results shown in Fig. 7 using these expressions leads to the conclusion that the final hydrate thickness decreases as the initial salt concentration in the meniscus increases.

5.5. Ion exclusion-salt precipitation-salt limited hydrate growth

The ionic concentration $C(h)$ in the free water that remains inside the hydrate shell increases during hydrate growth as a consequence of ion-exclusion; from mass concentration,

$C(h) = C_o [1 - (h/r)^2]$. The back analysis of experimental results in Fig. 7 shows that the molar concentration may reach salt saturation and salt may precipitate during hydrate growth.

On the other hand, ions and gas molecules compete for water, and the hydrate phase boundary shifts to lower temperature and higher pressure with increasing salt concentration [51–54,56,57]. Eventually, hydrate growth may stop for a given P–T condition. Our $P=8$ MPa and $T=275$ K conditions for CH_4 hydrate correspond to the phase boundary for a salt concentration of $c=4.0$ M [54]. We conclude that hydrate formation in our tests ended due to the high concentration of salt in the liquid water inside the hydrate shell. Low ionic and gas diffusive transport through the hydrate shell will render the gas–hydrate–brine system stable for relatively long periods.

6. Conclusions

Hydrate formation implies a pronounced transition from a condition of low gas concentration in water to a condition of high gas concentration in hydrate. In addition, the concentration of gas in water is lower in the presence of hydrate than in hydrate-free systems ($C_{ah} < C_{bh}$) and it is crystal size-dependent. These phenomena suggest complex nucleation and growth processes and anticipate the emergence of unexpected phenomena, including transient formation/ dissociation.

Rapid hydrate growth after the induction time consumes the excess gas ($C_{bh} - C_{ah}$) that dissolved by diffusive transport (the solubility of CO_2 in water is higher than that of CH_4 , therefore, a larger mass of CO_2 hydrate may form during early growth). Thereafter, diffusion at the tip of the hydrate mass causes dissolution. These processes explain transient formation–dissolution following early hydrate growth.

Experimentally observed fast growth rates cannot be justified by diffusive gas transport through the hydrate shell that separates the gas from the liquid water. We anticipate that successive hydrate formation and water–hydrate volume expansion create tensile discontinuities in the hydrate shell which facilitate gas transport.

Hydrate does not grow homogeneously as a planar front but advances in the form of lobes that invade the water phase. These lobes may correspond to the discontinuities in the hydrate shell. The early elongated topology observed in capillary tubes provides a higher surface and a shorter distance for diffusive gas transport from the bulk water. A short diffusive distance supports fast early hydrate growth.

Acknowledgments

Support for this research was provided by U.S. Department of Energy. Additional funding was provided by the Goizueta Foundation. We are grateful to Connor Barrett for proofreading the manuscript.

References

- [1] T.J. Kneafsey, L. Tomutsa, C.E. Taylor, A. Gupta, G. Moridis, B. Freifeld, Y. Seol, Methane hydrate formation and dissociation in a partially saturated sand 50 (2005) 33–35 American Chemical Society, Division of Petroleum Chemistry, Preprints 50 (2005) 33–35.
- [2] W.F. Waite, W.J. Winters, D.H. Mason, Methane hydrate formation in partially water-saturated Ottawa sand, American Mineralogist 89 (8–9) (2004) 1202–1207.
- [3] O.Y. Zatsepin, B.A. Buffet, Experimental study of stability of CO_2 hydrate in a porous medium, Fluid Phase Equilibria 200 (2) (2001) 263–275.
- [4] S. Circone, L.A. Stern, S.H. Kirby, The role of water in gas hydrate dissociation, Journal of Physical Chemistry B 108 (2004) 5747–5755.

- [5] T. Ebinuma, Y. Kamata, H. Minagawa, R. Ohmura, J. Nagao, H. Narita, Mechanical properties of sandy sediment containing methane hydrate, in: *Proceeding of the Fifth International Conference on Gas-Hydrate*, June 12–16, 2005, Trondheim, Norway, 2005.
- [6] V.A. Kamath, P.N. Mutalik, J.H. Sira, S.L. Patil, Experimental study of brine injection and depressurization methods for dissociation of gas hydrates, *SPE Formation Evaluation* 6 (1991) 477–484.
- [7] A. Masui, H. Haneda, Y. Ogata, K. Aoki, The effect of saturation degree of methane hydrates on the shear strength of synthetic methane hydrate sediments, in: *Proceeding of the Fifth International Conference on Gas-Hydrate*, June 12–16, 2005, Trondheim, Norway, 2005.
- [8] L.A. Stern, S.H. Kirby, W.B. Durham, Polycrystalline methane hydrate: synthesis from superheated ice, and low-temperature mechanical properties, *Energy & Fuels* 12 (1998) 201–211.
- [9] J.W. Ullrich, M.S. Selim, E.D. Sloan, Theory and measurement of hydrate dissociation, *AIChE Journal* 33 (1987) 747–752.
- [10] W.F. Waite, B.J. deMartin, S.H. Kirby, J. Pinkston, C.D. Ruppel, Thermal conductivity measurements in porous mixtures of methane hydrate and quartz sand, *Geophysical Research Letters* 9 (24) (2002).
- [11] J.-H. Yoon, T. Kawamura, Y. Yamamoto, T. Komai, Transformation of methane hydrate to carbon dioxide hydrate: in situ raman spectroscopic observations, *The Journal of Physical Chemistry A* 108 (2004) 5057–5059.
- [12] M. Hyodo, Y.N. Nakata, Yoshimoto, T. Ebinuma, Basic research on the mechanical behavior of methane hydratesediments mixture, *Soils Found* 45 (2005) 75–85.
- [13] T.S. Collett, Energy resource potential of natural gas hydrates, *A.A.P.G. Bulletin* 86 (11) (2002) 1971–1992.
- [14] E. Spangenberg, J. Kulenkampff, Physical properties of gas hydrate bearing sediments, in: *Proceedings of the Fifth International Conference on Gas Hydrates*, Trondheim, Norway, 2005.
- [15] Y. Zhong, R.E. Rogers, Surfactant effects on gas hydrate formation, *Chemical Engineering Science* 55 (19) (2000) 4175–4187.
- [16] J.W. Jung, J.C. Santamarina, K. Soga, Stress–Strain Response of Hydrate-Bearing Sediments: numerical Study Using DEM Simulations, under review (2011).
- [17] T.S. Yun, J.C. Santamarina, C. Ruppel, Mechanical properties of sand, silt, and clay containing tetrahydrofuran hydrate, *Journal of Geophysical Research* 112 (2007).
- [18] N.H. Fletcher, Active sites and ice crystal nucleation, *Journal of the Atmospheric Sciences* 26 (6) (1969) 1266.
- [19] D. Kashchiev, A. Firoozabadi, Nucleation of gas hydrates, *Journal of Crystal Growth* 243(3–4) (2002) 476–489.
- [20] B. Kvamme, A. Graue, T. Buanes, T. Kuznetsova, G. Erslund, Storage of CO₂ in natural gas hydrate reservoirs and the effect of hydrate as an extra sealing in cold aquifers, *International Journal of Greenhouse Gas Control* 1 (2007) 236–246.
- [21] M.R. Walsh, C.A. Koh, E.D. Sloan, A.K. Sum, D.T. Wu, Microsecond simulations of spontaneous methane hydrate nucleation and growth, *Science* 326 (2009) 1095–1098. doi:10.1126/science.1174010.
- [22] J.W. Jung, D.N. Espinoza, J.C. Santamarina, Properties and phenomena relevant to CH₄–CO₂ replacement in hydrate bearing sediments, *Journal of Geophysical Research—Solid Earth* 115 (2010) B10102. doi:10.1029/2009JB000812.
- [23] T. Mochizuki, T.H. Mori, Clathrate hydrate film growth along water/hydrate former phase boundaries—numerical heat-transfer study, *Journal of Crystal Growth* 290 (2006) 642–652.
- [24] R. Ohmura, T. Shigetomi, Y.H. Mori, Formation, growth and dissociation of clathrate hydrate crystals in liquid water in contact with a hydrophobic hydrate-forming liquid, *Journal of Crystal Growth* 196 (1999) 164–173.
- [25] M. Sugaya, Y.H. Mori, Behavior of clathrate hydrate formation at the boundary of liquid water and a fluorocarbon in liquid or vapor state, *Chemical Engineering Science* 51 (1996) 3505–3517.
- [26] C.J. Taylor, K.T. Miller, C.A. Koh, E.D. Sloan, Macroscopic investigation of hydrate film growth at the hydrocarbon/water interface, *Chemical Engineering Science* 62 (2007) 6524–6533.
- [27] T. Uchida, T. Ebinuma, J. Kawabata, H. Narita, Microscopic observations of formation processes of clathrate–hydrate films at an interface between water and carbon dioxide, *Journal of Crystal Growth* 204 (1999) 348–356.
- [28] T. Uchida, S. Takeya, Y. Kamata, I.Y. Ikeda, J. Nagao, T. Ebinuma, H. Narita, O. Zatssepina, B.A. Buffett, Spectroscopic observations and thermodynamic calculations on clathrate hydrates of mixed gas containing methane and ethane: determination of structure, composition and cage occupancy, *Journal of Physical Chemistry B* 106 (2002) 12426–12431.
- [29] E.M. Freer, M.S. Selim, S.E. D., Methane hydrate film growth kinetics, *Fluid Phase Equilibria* 185 (2001) 65–75.
- [30] P. Gayet, C. Dicharry, G. Marion, A. Graciaa, J. Lachaise, A. Nesterov, Experimental determination of methane hydrate dissociation curve up to 55 MPa by using a small amount of surfactant as hydrate promoter, *Chemical Engineering Science* 60 (2005) 5751–5758.
- [31] W. Lin, G.J. Chen, C.Y. Sun, X.Q. Guo, Z.K. Wu, M.Y. Liang, C.L. T., L.Y. Yang, Effect of surfactant on the formation and dissociation kinetic behavior of methane hydrate, *Chemical Engineering Science* 59 (2004) 4449–4455.
- [32] D.D. Link, E.P. Ladner, H.A. Elsen, C.E. Taylor, Formation and dissociation studies for optimizing the uptake of methane by methane hydrates, *Fluid Phase Equilibria* 211 (2003) 1–10.
- [33] R. Ohmura, S. Kashiwazaki, Y.H. Mori, Measurement of clathrate hydrate film thickness using laser interferometry, *Journal of Crystal Growth* 218 (2000) 372–380.
- [34] R. Ohmura, W. Shimaday, T. Uchida, Y.H. Mori, S. Takeyay, J. Nagaoy, H. Minagaway, T. Ebinumay, H. Naritay, Clathrate hydrate crystal growth in liquid water saturated with a hydrate-forming substance: variations in crystal morphology, *Philosophical Magazine* 84 (2004) 1–16.
- [35] S. Subramanian, E.D. Sloan, Solubility effects on growth and dissolution of methane hydrate needles, in: *Proceedings of the Fourth International Conference on Gas Hydrates*, Yokohama, (2002), pp. 856–861.
- [36] Y. Tabe, S. Hirai, K. Okazaki, Massive CO₂ clathrate hydrate growth at a high-polar-energy surface, *Journal of Crystal Growth* 220 (2000) 180–184.
- [37] C.J. Taylor, K.T. Miller, C.A. Koh, E.D. Sloan, Macroscopic investigation of hydrate film growth at the hydrocarbon/water interface, *Chemical Engineering Science* 62 (2007) 6524–6533.
- [38] A.R. Thomas, Royal commission on medical education, *British Medical Journal* 2 (1965) 423. &
- [39] Pa Withersp, L. Bonoli, Correlation of diffusion coefficients for paraffin, aromatic, and cycloparaffin hydrocarbons in water, *Industrial and Engineering Chemistry Fundamentals* 8 (1969) 589. &
- [40] N. Davies, C. Fear, A novel approach to harvesting of cultured cells from prenatal samples resulting in high mitotic index and rapid re-growth of cultures, *Journal of Medical Genetics* 41 (2004). S51–S51.
- [41] D.L. Zhong, D.P. Liu, Z.M. Wu, L. Zhang, Natural gas hydrate formation and growth on suspended water droplet, in: *Proceedings of the Sixth International Conference on Gas Hydrates (ICGH 2008)*, Vancouver, British Columbia, Canada, July 6–10, 2008. (2008).
- [42] G. Rehder, S.H. Kirby, W.B. Durham, L.A. Stern, E.T. Peltzer, J. Pinkston, P.G. Brewer, Dissolution rates of pure methane hydrate and carbon dioxide hydrate in undersaturated seawater at 1000-m depth, *Geochimica et Cosmochimica Acta* 68 (2004) 285–292.
- [43] Y. Zhang, Z. Xu, Kinetics of convective crystal dissolution and melting with applications to methane hydrate dissolution and dissociation in seawater, *Earth and Planetary Science Letters* 213 (2003) 133–148.
- [44] W.F. Waite, J.C. Santamarina, D.D. Cortes, B. Dugan, D.N. Espinoza, J. Germaine, J. Jang, J.W. Jung, T.J. Kneafsey, H. Shin, K. Soga, W.J. Winters, T.-S. Yun, Physical properties of hydrate-bearing sediment, *Reviews of Geophysics* 47 (2009). RG4003.
- [45] I. Aya, K. Yamane, H. Nariai, Solubility of CO₂ and density of CO₂ hydrate at 30 MPa, *Energy* 22 (1997) 263–271.
- [46] M.K. Davie, O.Y. Zatssepina, B.A. Buffett, Methane solubility in marine hydrate environments, *Marl Geology* 203 (2004) 177–184.
- [47] P. Servio, P. Englezos, Measurement of dissolved methane in water in equilibrium with its hydrate, *Journal of Chemical Engineering Data* 47 (2002) 87–90.
- [48] Z. Duan, R. Sun, An improved model calculating CO₂ solubility in pure water and aqueous NaCl solutions from 273 to 533 K and from 0 to 2000 bar, *Chemical Geology* 193 (2003) 257–271.
- [49] S.A. Klapp, H. Klein, W.F. Kuhs, First determination of gas hydrate crystallite size distributions using high-energy synchrotron radiation, *Geophysical Research Letter* 34 (2007) L13608.
- [50] S.A. Klapp, S. Hemes, H. Klein, G. Bohrmann, I. MacDonald, W.F. Kuhs, Grain size measurements of natural gas hydrates, *Marl Geology* 274 (2010) 85–94.
- [51] S. Duan, R. Sun, A model to predict phase equilibrium of CH₄ and CO₂ clathrate hydrate in aqueous electrolyte solutions, *American Mineralogist* 91 (2006) 1346–1354.
- [52] R. Masoudi, B. Tohidi, A. Danesh, A.C. Todd, R. Anderson, R.W. Burgass, J.H. Yang, Measurement and prediction of gas hydrate and hydrated salt equilibria in aqueous ethylene glycol and electrolyte solutions, *Chemical Engineering Science* 60 (2005) 4213–4224.
- [53] A.H. Mohammadi, B. Tohidi, Prediction of hydrate phase equilibria in aqueous solutions of salt and organic inhibitor using combined equation of state and activity coefficient-based model, *The Canadian Journal of Chemical Engineering* 83 (2005) 865–871.
- [54] K.K. Østergaard, R. Masoudi, B. Tohidi, A. Danesh, A.C. Todd, A general correlation for predicting the suppression of hydrate dissociation temperature in the presence of thermodynamic inhibitors, *Journal of Petroleum Science and Engineering* 48 (2005) 70–80.
- [55] J.W. Jung, J.C. Santamarina, CH₄–CO₂ replacement in hydratebearing sediments: a pore-scale study, *Geochemistry, Geophysics, Geosystems* (2010). doi:10.1029/2010GC003339. Q0AA13.
- [56] X. Liu, P.B. Flemings, Passing gas through the hydrate stability zone at southern Hydrate Ridge, offshore Oregon, *Earth and Planetary Science Letters* 241 (2006) 211–226.
- [57] X. Liu, P.B. Flemings, Dynamic multiphase flow model of hydrate formation in marine sediments, *Journal of Geophysical Research* 112 (2007).